

This is a repository copy of *Vlasov-Fokker-Planck simulations of pre-magnetized ablating planar targets*.

White Rose Research Online URL for this paper:

<https://eprints.whiterose.ac.uk/195990/>

Version: Published Version

Article:

Hill, D. W., Ridgers, C. P. orcid.org/0000-0002-4078-0887, Kingham, R. J. et al. (1 more author) (2021) Vlasov-Fokker-Planck simulations of pre-magnetized ablating planar targets. *Physics of Plasmas*. 092708. ISSN 1089-7674

<https://doi.org/10.1063/5.0049685>

Reuse

This article is distributed under the terms of the Creative Commons Attribution (CC BY) licence. This licence allows you to distribute, remix, tweak, and build upon the work, even commercially, as long as you credit the authors for the original work. More information and the full terms of the licence here:

<https://creativecommons.org/licenses/>

Takedown

If you consider content in White Rose Research Online to be in breach of UK law, please notify us by emailing eprints@whiterose.ac.uk including the URL of the record and the reason for the withdrawal request.

Vlasov–Fokker–Planck simulations of pre-magnetized ablating planar targets

Cite as: Phys. Plasmas **28**, 092708 (2021); <https://doi.org/10.1063/5.0049685>

Submitted: 08 March 2021 • Accepted: 31 August 2021 • Published Online: 21 September 2021

 D. W. Hill,  C. P. Ridgers,  R. J. Kingham, et al.

COLLECTIONS

 This paper was selected as an Editor's Pick



View Online



Export Citation



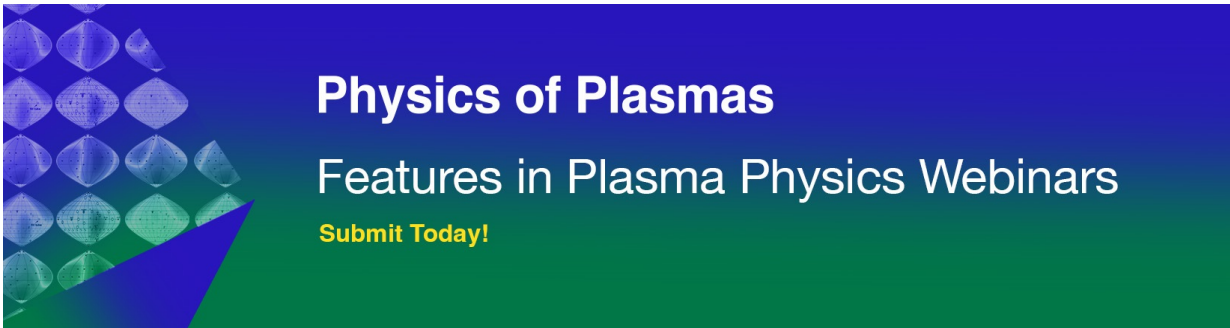
CrossMark

ARTICLES YOU MAY BE INTERESTED IN

[Biermann battery magnetic fields in ICF capsules: Total magnetic flux generation](#)
Phys. Plasmas **28**, 092705 (2021); <https://doi.org/10.1063/5.0059366>

[Achieving record hot spot energies with large HDC implosions on NIF in HYBRID-E](#)
Phys. Plasmas **28**, 072706 (2021); <https://doi.org/10.1063/5.0047841>

[Deep-learning-enabled Bayesian inference of fuel magnetization in magnetized liner inertial fusion](#)
Phys. Plasmas **28**, 092701 (2021); <https://doi.org/10.1063/5.0056749>



Physics of Plasmas
Features in Plasma Physics Webinars
[Submit Today!](#)

Vlasov–Fokker–Planck simulations of pre-magnetized ablating planar targets

Cite as: Phys. Plasmas **28**, 092708 (2021); doi: [10.1063/5.0049685](https://doi.org/10.1063/5.0049685)

Submitted: 8 March 2021 · Accepted: 31 August 2021 ·

Published Online: 21 September 2021



View Online



Export Citation



CrossMark

D. W. Hill,^{1,2}  C. P. Ridgers,^{1,a)}  R. J. Kingham,²  and C. A. Walsh² 

AFFILIATIONS

¹York Plasma Institute, Department of Physics, University of York, Heslington York, North Yorkshire, YO10 5DD, United Kingdom

²Blackett Laboratory, Imperial College, London SW7 2AZ, United Kingdom

^{a)}Author to whom correspondence should be addressed: christopher.ridgers@york.ac.uk

ABSTRACT

Magnetic fields, spontaneously generated around laser heating nonuniformities, have been found to invert and enhance electron pressure perturbations in the conduction zones of laser-produced plasmas without applied magnetic fields. The application of a sufficiently strong magnetic field is predicted to damp this phenomenon, but may instead result in magneto-thermal instability. Two-dimensional Vlasov–Fokker–Planck simulations of the conduction zone of laser-produced plasmas, subject to externally applied magnetic fields of different field strengths, are performed. The effects of non-locality upon extended collisional transport terms and instability thresholds are investigated. It is found that magnetized transport terms Righi–Leduc heat flow and thermoelectric heat flow are strongly enhanced by non-locality (up to twofold), even at the top of the temperature gradient, due to larger magnetization of the mediating hot electrons (relative to their thermal counterparts). Meanwhile, the Nernst effect efficiently advects magnetic field out of the conduction zone before instability (which requires Hall parameters, $\chi > 0.1$) can take hold.

© 2021 Author(s). All article content, except where otherwise noted, is licensed under a Creative Commons Attribution (CC BY) license (<http://creativecommons.org/licenses/by/4.0/>). <https://doi.org/10.1063/5.0049685>

I. INTRODUCTION

The application of an external magnetic field to an inertial-confinement-fusion (ICF) target presents a promising method for improving the neutron yield.¹ Improvements in fusion performance are attributed to the embedded magnetic flux inhibiting heat losses. In order to attain this compressed, hot spot state, the fuel capsule must first undergo the process of laser ablation. In the ablation phase, the outer surface of the fuel capsule is ionized and heated by the laser drive, forming a rapidly expanding coronal plasma. The rapid thermal expansion causes a reactionary force, manifesting as a hydrodynamic (ablation) pressure that compresses the fuel capsule. To maintain the ablation pressure, energy must be efficiently conducted from the hot, low density plasma at the critical surface, where the energy is absorbed, to the ablation surface, the point of peak pressure at the cold, solid density target surface. The presence of an external magnetic field may both inhibit thermal conduction in this region, perpendicular to the field direction,² and seed field-generating thermal³ and magneto-thermal⁴ instabilities around inhomogeneities in the laser-energy deposition.

It has long been known that the conditions within this conduction zone, the region between the critical and ablation surfaces, are far

from local thermodynamic equilibrium (LTE).⁵ The collisional mean-free-paths of the heat carrying electrons are on the order of the temperature scale length, $L_T = T_{e,0}/\partial_x T_{e,0}$. The electron thermal transport is non-local; the thermal conduction cannot be described by a Fick-type law, dependent only on the local temperature gradient, ∇T_e , and the Braginskii thermal conductivity, κ :² $\mathbf{q} = -\kappa \nabla T_e$. Magnetic fields strongly effect non-locality and vice versa^{6–10} and their interplay in magnetized ICF implosions is poorly understood.¹¹

Previously, it was shown that magnetic fields spontaneously generated around nonuniformities in laser absorption could result in an inversion and enhancement of pressure perturbations within the conduction zone.⁹ The phenomenon was due to the sideways deflection of heat flow in the conduction zone by the magnetic field, the Righi–Leduc effect. For sufficiently strong Hall parameters ($\chi \gtrsim 0.1$), the direction of Righi–Leduc heat flow reverses along magnetization gradients. It is predicted that under such conditions, phase inversion should be suppressed. These conditions, however, may instead result in instability.^{3,4} Nevertheless, the true conduction zone dynamics remain unclear, as assumptions included in instability growth rate calculations are not valid in the steep gradients of the conduction zone.

In this paper, we present two-dimensional (2D) Vlasov–Fokker–Planck simulations of a planar, ablating CH foil, subject to an externally applied, out-of-plane magnetic field. Three applied magnetic field strengths are used: 0, 50, and 400 T. The laser heating profile is modulated with a transverse sinusoidal perturbation which takes the form $I(x) = I_0(x)(1 + \alpha e^{i(2\pi y/\lambda_p)})$ and the perturbation wavelength is $\lambda_p = 5 \mu\text{m}$. Modulations between 1% and 100% ($\alpha = 0.01 - 1$) are examined. The phenomenology between the two limits are similar; thus in general, only the 1% case will be discussed here. In Sec. IV A, the effects of non-locality on transport are examined in one dimension. In Sec. IV B, the effects of applied magnetic field upon the perturbation evolution are investigated. Finally, the effects of non-locality on transverse heat flow are examined in Sec. IV E.

II. THEORETICAL BACKGROUND

The dynamics of electrons in a semi-collisional plasma is well described by the Vlasov–Fokker–Planck equation,

$$\left[\frac{\partial}{\partial t} + \mathbf{v} \cdot \frac{\partial}{\partial \mathbf{r}} + \frac{e}{m_e} (\mathbf{E} + \mathbf{v} \times \mathbf{B}) \cdot \frac{\partial}{\partial \mathbf{v}} \right] f(\mathbf{v}, \mathbf{r}, t) = - \frac{\partial}{\partial \mathbf{v}} \cdot \{ f(\mathbf{v}, \mathbf{r}, t) \langle \Delta \mathbf{v} \rangle \} + \frac{1}{2} \frac{\partial}{\partial \mathbf{v}} \frac{\partial}{\partial \mathbf{v}} : \{ f(\mathbf{v}, \mathbf{r}, t) \langle \Delta \mathbf{v} \Delta \mathbf{v} \rangle \}, \quad (1)$$

where \mathbf{E} and \mathbf{B} represent the macroscopic electric and magnetic fields. In order to make this equation more tractable, it is standard to expand the electron distribution function, $f(\mathbf{v}, \mathbf{r}, t)$, in Cartesian tensors,¹² $f(\mathbf{v}, \mathbf{r}, t) = f_0(v, \mathbf{r}, t) + \underline{\mathbf{f}}_1(v, \mathbf{r}, t) \cdot \hat{\mathbf{v}} + \dots$ (where $\hat{\mathbf{v}}$ is the velocity unit vector). Higher order terms in this expansion represent increasing degrees of velocity anisotropy, and are increasingly damped away by the effects of collisions [the right-hand side operator of Eq. (1)].

In the limit that the plasma is sufficiently collisional to attain thermodynamic equilibrium, the distribution function takes the form of a Maxwellian distribution function, $f_0(v, \mathbf{r}, t) \rightarrow (n_e / (\pi^{3/2} v_{th}^3)) e^{-v^2/v_{th}^2}$ (where n_e and T_e are the electron number density and temperature while v_{th} is the electron thermal velocity, $v_{th} = \sqrt{2k_b T_e / m_e}$). Velocity moments of Eq. (1) may be used to derive a simpler set of equations. The resultant equations describe transport in a collisional plasma and are known as Ohm’s law and the heat flow equation,

$$\mathbf{q} = - \frac{n_e T_e \tau_B}{m_e} \underline{\kappa}^c \cdot \nabla T_e - \frac{T_e}{e} \left(\underline{\beta}^c + \frac{5}{2} \right) \cdot \mathbf{j}, \quad (2)$$

$$\mathbf{E} = - \frac{\nabla P_e}{en_e} + \frac{1}{en_e} \mathbf{j} \times \mathbf{B} + \frac{m_e}{e^2 n_e \tau_B} \underline{\alpha}^c \cdot \mathbf{j} - \frac{1}{e} \underline{\beta}^c \cdot \nabla T_e. \quad (3)$$

Here, \mathbf{q} and \mathbf{j} are the total heat flux and the current density, respectively. Meanwhile, n_e is the electron number density, P_e the electron pressure, and τ_B the collision time. $\underline{\alpha}$, $\underline{\kappa}$, and $\underline{\beta}$ are the dimensionless resistive, conductive, and thermo-electric transport coefficients, respectively.¹³

These equations, owing to their intuitive nature and ease of computational implementation, are widely used in current laser-plasma computational modeling. There are several physical effects described in Eq. (3) that are key to this work. In the presence of a temperature gradient, magnetic flux will be advected with the hot electrons, responsible for the diffusive heat flow, the Nernst effect,

$$\partial_t \mathbf{B} = \nabla \times \left[\underline{\beta} \cdot \nabla T_e \right] \quad (4)$$

$$= \nabla \times (\mathbf{v}_N \times \mathbf{B}) + (\nabla \beta_{\perp} \times \nabla T_e), \quad (5)$$

where $\mathbf{v}_N = -\beta_{\perp} \nabla T_e / |\mathbf{B}|$ is the Nernst velocity. Heat flow directed down a temperature gradient will be deflected by the Lorentz force generated by a perpendicular magnetic field. The additional “transverse” component is called the Righi–Leduc heat flow, \mathbf{q}_{RL} ,

$$\mathbf{q}_{RL} = -\kappa_{\perp} (\mathbf{b} \times \nabla T_e), \quad (6)$$

where $\mathbf{b} = \mathbf{B} / |\mathbf{B}|$. For conditions where the temperature scale length $L_T = T_e / \partial_x T_e \lesssim 80 \lambda_{mfp}$, the assumption of thermodynamic equilibrium connecting Eqs. (1) and (6) begins to break down. The relationship between the local driving forces, ∇T_e , \mathbf{j} , etc., and transport phenomena in Eqs. (3)–(6) becomes more tenuous. Heat and electric field transport instead becomes mediated by the dynamics of the hot ($v \sim 2v_{th} - 4v_{th}$), relatively collisionless population of electrons in the distribution function tail. The electron mean-free-path, λ_{mfp} , scales with velocity as $\lambda_{mfp} \propto v^4$; consequently these electrons are non-local, they influence transport over much longer length scales than expected under equilibrium assumptions. Not only do the $2v_{th} - 4v_{th}$ electrons travel 16 – 256 times further between collisions, but they are also 8 – 64 times more magnetized, as the Hall parameter $\chi = \omega \tau_{ei} \propto v^3$.

In this paper, we investigate this interim limit between Eqs. (1) and (3) in which non-locality becomes important. Many intermediate models have been used to incorporate non-locality into integrated hydrocode modeling.^{14–16} Although these reduced non-local models have demonstrated some success in predicting the non-local heat flow,^{17–19} they, however, cannot track the evolution of the non-local electron population,¹⁹ and are yet to be benchmarked in magnetized settings. For a more complete description of a non-local transport phenomenon, the full electron Vlasov–Fokker–Planck equation must be solved which we choose to do here. The role of different transport phenomena may then be reconstructed from generalized versions of the Ohm’s law and heat flow equation,^{20,21} not involving assumptions of thermodynamic equilibrium.

III. SIMULATION SETUP

Simulations of a planar CH target irradiated by an $I = 800 \text{ TW/cm}^2$, $\lambda = 0.35 \mu\text{m}$ laser beam were performed using the Vlasov–Fokker–Planck (VFP) code IMPACT.²² Laser heating was simulated using a static inverse bremsstrahlung heating operator,²³ modulated by a transverse sinusoidal perturbation. The initial profiles are displayed in Fig. 1(a). The simulations were initialized with three different externally applied magnetic field strengths of 0, 50, and 400 T. The magnetic field vector is directed perpendicular to the simulation plane.

IMPACT solves the electron VFP equation, Eq. (1), in two Cartesian spatial dimensions and three velocity space dimensions using implicit finite-difference methods. Faraday’s and Ampère’s laws are solved self-consistently to obtain the electromagnetic fields, $(E_x, E_y, 0)$ and $(0, 0, B_z)$, while a magneto-hydrodynamic momentum equation is used to model the cold ions. Standard Cartesian tensor expansion¹² is used to expand the electron distribution function, $f(\mathbf{v}, \mathbf{r}, t) = f_0(v, \mathbf{r}, t) + \underline{\mathbf{f}}_1(v, \mathbf{r}, t) \cdot \hat{\mathbf{v}} + \dots$ (where $\hat{\mathbf{v}}$ is the velocity unit vector), in increasing degrees of velocity anisotropy. Collisions increasingly smooth out higher order terms in this expansion, $f_0 \gg \underline{\mathbf{f}}_1 \gg \underline{\mathbf{f}}_2$, etc. The plasmas considered here are sufficiently collisional that we can truncate this expansion at $\underline{\mathbf{f}}_1$. Here, $\mathbf{r} = (x, y)$ is the Cartesian spatial coordinate. In reality, the ablation of a plasma slab is a 3D phenomenon. Our VFP simulations are, however, limited to two

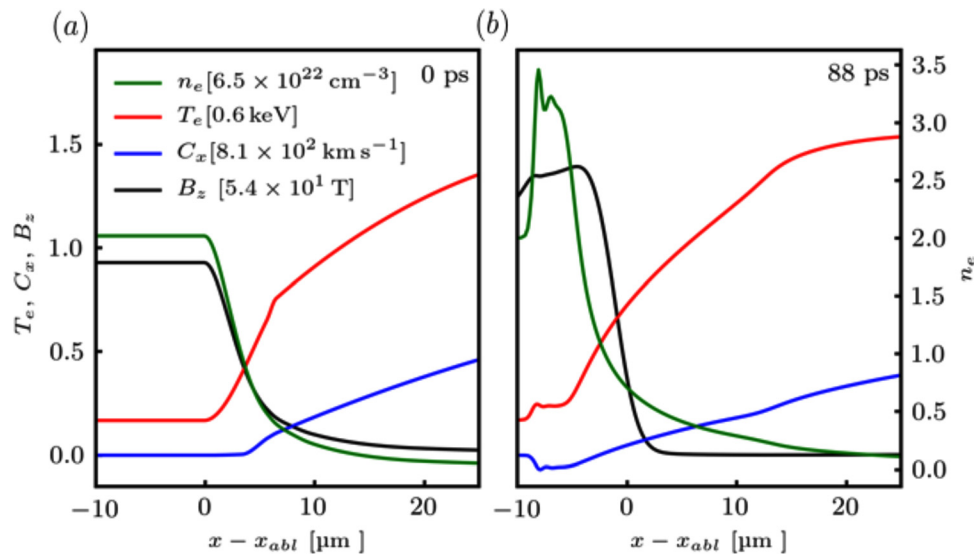


FIG. 1. Lineouts of electron number density, n_e ; electron temperature, T_e ; ion flow velocity, C_x ; and the perpendicular (z direction) magnetic field, B_z , for a 50 T applied field 1D IMPACT simulation. Initial profiles are presented in (a) while (b) shows lineouts after 88 ps. For orientation, the conduction zone is the region between the ablation front (where $C_x > 0$) and the critical surface where the laser energy is absorbed ($n_e = 9.1 \times 10^{21} \text{ cm}^{-3}$).

Cartesian spatial dimensions. This is sufficient to investigate the evolution of perturbations to the magnetic field phenomenologically.

A Thomas–Fermi equation of state model was used to model the effective ionization state of the plasma, $\langle Z \rangle$, which was dynamically updated using the plasma density ρ and electron temperature T_e . Electrons injected through ionization processes were assumed cold. The ionization source term takes the form $S = \partial_t Z n_i / (4\pi v^2) \delta(\mathbf{v})$, where $\partial_t Z$ represents the rate of change of effective atomic number, n_i is the ionic number density, and $\delta(\mathbf{v})$ is the Dirac delta function centered at velocity zero.

The conduction zone grid cell size is $\Delta x = \Delta y = 0.16 \mu\text{m}$ and the simulation time step is $\Delta t = 1.8 \times 10^{-14} \text{ s}$. A linearly increasing grid spacing is used in the corona and solid slab to ensure that the simulation boundary is located far from the domain of interest. The velocity grid consists of 200 grid points extending up to a maximum velocity of $v = 20 v_{th}$ [where the grid spacing increases exponentially and the reference thermal velocity is defined as $v_{th} = \sqrt{2e(740 \text{ eV})/m_e}$]. As IMPACT cannot simulate sharp material boundaries, we choose initial profiles for the macroscopic physical quantities assuming some ablation of the target has already taken place (see Fig. 1).

IV. RESULTS

A. One-dimensional evolution

In this section, the effect of the applied magnetic field on non-locality and transport is explored in one dimension. The initial profiles and those after 88 ps are displayed in Fig. 1. The magnetic field is advected out of the conduction zone and compressed into the ablation surface by the Nernst effect. Figure 2 displays the IMPACT electron distribution function for a 50 T simulation. Figure 2(a) displays $f_0(v)$ sampled from a point at the base of the conduction zone temperature gradient while in Fig. 2(b) $f_0(v)$ is taken from the top of the temperature gradient. The relatively collisionless electrons (those with velocities in the range $v = 2 v_{th} - 4 v_{th}$) diffuse down the temperature

gradient at a much faster rate than their colder, $v \sim v_{th}$, counterparts. The high velocity f_0 tail becomes depleted at the top of the temperature gradient (b), close to the critical surface and enhanced at the base (a), in the cold dense plasma around the ablation surface, $x \sim 0 \mu\text{m}$. It is well documented that this can cause suppression of transport at the top of the temperature gradient “flux-suppression” and enhancement at the base, for the Nernst term,^{24,25} Righi–Leduc heat flow²⁶ and diffusive heat flow⁵ (although maybe less of an effect for resistivity²¹). In addition, it is known that the heating of plasma by inverse bremsstrahlung also distorts the electron distribution away from Maxwellian.²³ This can also affect the transport coefficients²⁷ and so the growth of instabilities²⁸ and is included in our simulations.

Figure 3 displays the lineouts of the local (assuming thermodynamic equilibrium, dashed lines) and kinetic (solid lines) predictions for transport terms driven by the bulk temperature, $\partial_x T_e$, and magnetic field, $\partial_x B_z$, gradients in the conduction zone; the diffusive heat flow, $q_{\perp,x}$, Nernst velocity, $v_{N,x}$, transverse Righi–Leduc heat flow, $q_{RL,y}$, and transverse thermo-electric heat flow, $q_{E,y}$, terms. The solid black line denotes the zeroth order temperature (top) and magnetic field (bottom) profiles for reference. The Nernst and diffusive heat flow deviations from local predictions are qualitatively similar. Non-locality results in a greater than twofold enhancement of the Righi–Leduc [Fig. 3(c)] and thermo-electric [$\mathbf{q}_E = -\underline{\beta} \cdot \mathbf{j}_{T_e}$, Fig. 3(d)] heat flows. This is because these heat flow terms are largest in regions of high magnetic field strength, close to the ablation surface. The regions of high field strength coincide with an enhanced high velocity f_0 electron tail, resulting in a corresponding q_{RL} and q_E augmentation.

Magnetic field restricts the diffusion of electrons perpendicular to its field lines. Higher velocity electrons, in the distribution function tail, are relatively more magnetized than their thermal counterparts, $\chi = \omega \tau_{ei} \propto v^3$. For the 400 T applied field simulation, the field has been compressed to 500 T at the ablation surface by the Nernst effect.

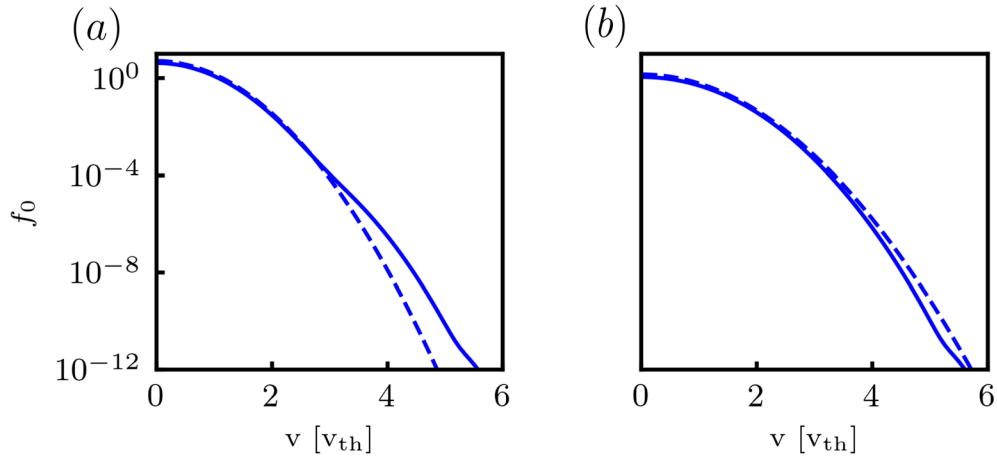


FIG. 2. Isotropic component of the electron distribution function, $f_0(v)$, sampled from 50 T applied field, 1D IMPACT simulation after 130 ps of evolution. f_0 is displayed at two example points in the conduction zone (a) at the base of the temperature gradient and (b) at the top of the temperature gradient. Dashed blue line is the equivalent equilibrium form for an electron distribution with the same temperature given for reference. (a) The electron high velocity tail is enhanced relative to equilibrium; (b) the high velocity tail is suppressed relative to equilibrium (a dearth of high velocity electrons at the top of the temperature gradient). Velocity is normalized in terms of the reference thermal velocity, $v_{th} = \sqrt{(2T_{e,0}/m_e)}$ where $T_{e,0} = 740$ eV.

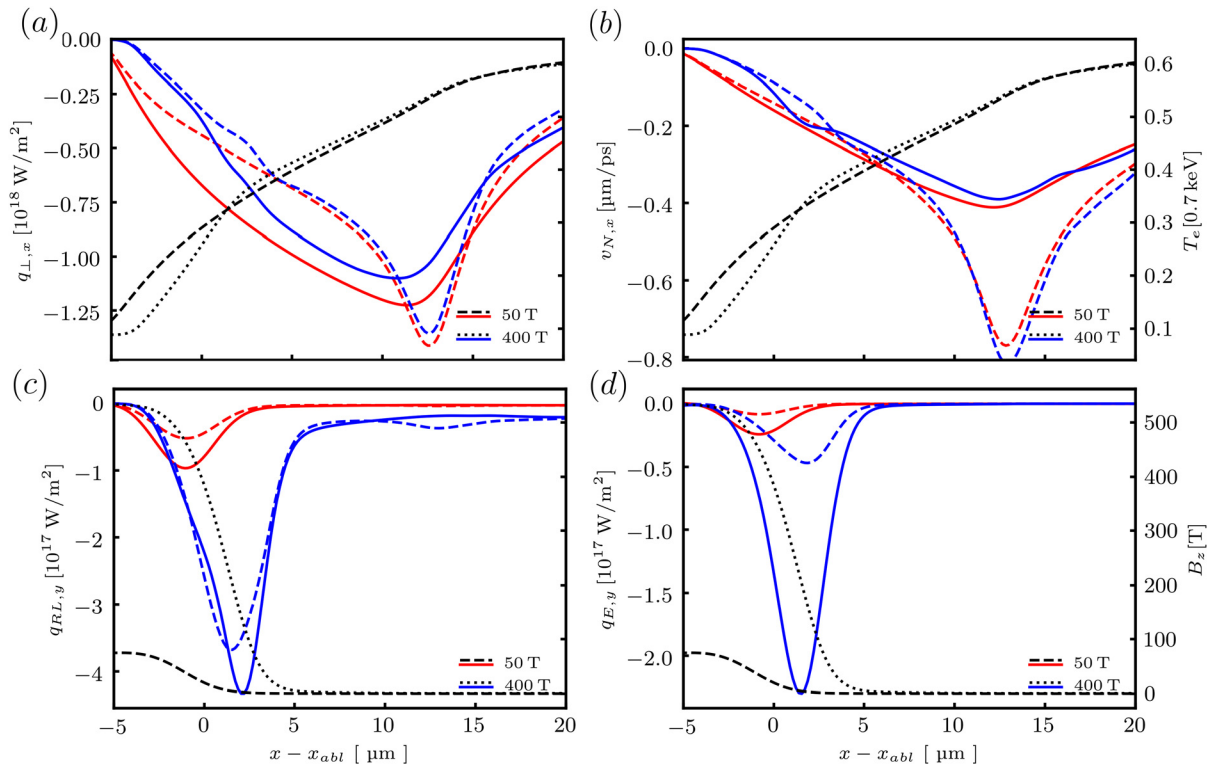


FIG. 3. Terms driven by $\partial_x T_e$ and $\partial_x B_z$. Lineouts of kinetic (solid lines) and classical/local (dashed lines) heat flow and Nernst components for two different applied field strengths after 35 ps of simulation time. (a) Displays longitudinal diffusive heat flow, $q_{\perp,x}$ and (b) the longitudinal Nernst velocity, $v_{N,x}$; (c) displays transverse Right-Leduc heat flow and (d) the transverse thermo-electric heat flow, $q_{E,y}$. Black lines denote lineouts of the temperature and magnetic field for reference.

This field strength is sufficiently large to relocalize the hot electron pre-heat at the base of the temperature gradient, $q_{\perp,k}/q_{\perp,c} \rightarrow 1$, close to the ablation surface, $x \sim 0 \mu\text{m}$. Interestingly, while the Nernst, diffusive heat flow and Righi–Leduc heat flow are effectively localized by this high field strength at $x - x_{abl} \rightarrow 0$, the thermo-electric heat flow, $q_{E,y}$, blue line in (d) exhibits a fourfold enhancement relative to its classical counterpart.

B. Two-dimensional evolution

The Nernst effect efficiently advects magnetic field out of the conduction zone into the cold collisional region around the ablation surface. As a result, Hall parameters in the conduction zone remain consistently below the $\chi \sim 0.1$ threshold required to initialize the field-generating thermal or magneto-thermal instabilities. Nevertheless, self-generated fields still play a dominant role in determining the δT_e evolution. Figure 4(a) displays the evolution of δT_e as a function of distance away from the ablation surface. Lineouts of $\delta T_e(y)$ at various $x - x_{abl}$ positions are presented for the 0, 50, and 400 T applied field simulations in Figs. 4(b)–4(d). Self-generated fields drive a Righi–Leduc heat flow, $\delta q_{y,RL} \propto -\frac{\partial \kappa_{\perp,0}}{\partial \chi} \partial_x T_{e,0} \delta \chi$, which deflects heat from $\delta \chi$ peaks to troughs. In the 0 and 50 T simulations, this heat flux inverts the δT_e (and thereby the δP_e) amplitude.⁹ The point at which this phase inversion occurs is indicated by the $|\delta T_e|$ cusp at $x - x_{abl} \approx 10 \mu\text{m}$ in Fig. 4(a). The 400 T simulation does not exhibit phase inversion. For sufficiently high magnetization, the direction of $\delta q_{y,RL}$ reverses ($\frac{\partial \kappa_{\perp,0}}{\partial \chi} < 0$), redirecting heat from $\delta \chi$ troughs to peaks, enhancing the incumbent δT_e . A linear model for the phase inversion is presented in Sec. IV C and Appendix.

In 50 and 400 T simulations, the phase of δT_e shifts with distance into the conduction zone. This phase shift is predominantly caused by

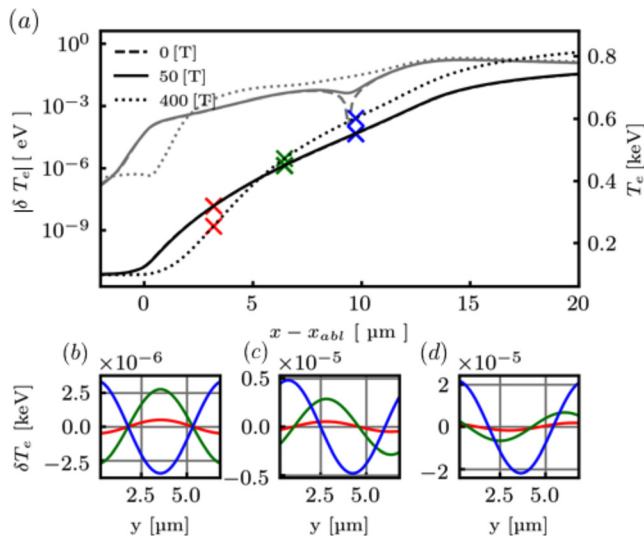


FIG. 4. (a) δT_e (grey lines) and zeroth order T_e (black lines) as a function of distance away from the ablation surface for different applied field strengths (the different line styles). (b), (c), and (d) display lineouts of δT_e in the transverse direction, sampled at the corresponding colored crosses in (a), for a 0 T simulation (b), a 50 T applied field simulation (c), and a 400 T simulation (d).

the zeroth order $q_{RL} \propto ik \frac{\partial \kappa_{\perp,0}}{\partial \chi} \tau_{ei,0} n_0 B_{z,0} (l_B - l_n)$ (where $l_x = \partial_x \alpha_0 / \alpha_0$ and $\alpha = n_e, B_z$), which is driven by the bulk magnetic field and density gradients, redirecting heat in the y direction.

At the same time, the deflected electrons responsible for the Righi–Leduc heat flow drag magnetic field lines along with them. This magnetic field advection is the cross-gradient Nernst effect, $\mathbf{v}_N = -\beta_{\perp} (\mathbf{b} \times \nabla T_e)$, and is predicted to result in significant magnetic field line twisting in pre-magnetized ICF experiments.²⁹

C. A heuristic model for δT_e conduction zone evolution

The conduction zone evolution of δT_e may be explained through linear perturbation theory. The induction equation for the magnetic field and the steady-state temperature equation subject to sinusoidally perturbed heating, $\nabla \cdot \mathbf{q} = (I + \delta I e^{iky}) \delta(x - x_c)$, are used to describe the system. Perturbations in magnetic field and temperature are assumed to take the form $T_e = T_{e,0}(x) + \delta T(x) e^{iky}$, $B_z = B_{z,0}(x) + \delta B_z(x) e^{iky}$. Upon linearizing, the following equations are arrived at, to first order:

$$(\delta_1 + \delta_2 \partial_x^2)(T_0^{5/2} \delta T) + \epsilon_1 \delta B_z = 0, \quad (7)$$

$$(\eta_1 + \eta_2 \partial_x + \eta_3 \partial_x^2)(T_0^{5/2} \delta T) + (\gamma_1 + \gamma_2 \partial_x + \gamma_3 \partial_x^2) \delta B_z = 0, \quad (8)$$

where the coefficients are given by

$$\begin{aligned} \delta_1 &= -\kappa_{\perp,0} k^2 + ik \frac{\partial \kappa_{\perp,0}}{\partial \chi} \tau_{ei,0} n_0 B_{z,0} (l_B - l_n), \\ \delta_2 &= \kappa_{\perp,0}, \\ \epsilon_1 &= -ik \frac{\partial \kappa_{\perp,0}}{\partial \chi} \theta_0 T_0^{5/2}, \\ \eta_1 &= \frac{ik}{T_0^{5/2}} l_n + \alpha_0 \frac{B_{z,0}}{T_0^{7/2}} \left(\frac{15}{2} l_T l_B - \frac{3}{2} l_{2B} \right) + \frac{\partial \beta_{\perp,0}}{\partial \chi} \frac{\tau_B B_{z,0}}{n_0 T_0} \\ &\quad \times (k^2 + l_B l_T - l_n l_T - 2l_T^2 + l_{2T}), \\ \eta_2 &= -\frac{3}{2} \alpha_0 \frac{B_{z,0}}{T_0^{7/2}} l_B + \frac{\partial \beta_{\perp,0}}{\partial \chi} \frac{\tau_B B_{z,0}}{n_0 T_0} (2l_T + l_n - l_B), \\ \eta_3 &= -\frac{\partial \beta_{\perp,0}}{\partial \chi} \frac{\tau_B B_{z,0}}{n_0 T_0}, \\ \epsilon_1 &= -ik \frac{\partial \kappa_{\perp,0}}{\partial \chi} \theta_0 T_0^{5/2}, \\ \gamma_1 &= \left[\partial_x C_{x,0} + \alpha_0 k^2 - \frac{\partial \beta_{\perp,0}}{\partial \chi} \partial_x \theta_0 \right], \\ \gamma_2 &= \left[C_{x,0} - \frac{\partial \beta_{\perp,0}}{\partial \chi} \theta_0 + \frac{3}{2} \alpha_0 \frac{\partial_x T_0}{T_0} \right], \\ \gamma_3 &= -\alpha_0, \end{aligned} \quad (10)$$

and

$$\alpha_0 = \frac{\alpha_{\perp,0} \delta_c^2}{T_0^{3/2}}, \quad \theta_0 = \tau_{ei,0} \partial_x T_0,$$

$$l_{\zeta} = \frac{\partial_x \zeta_0}{\zeta_0}, \quad \text{and} \quad l_{2,\zeta} = \frac{\partial_x^2 \zeta_0}{\zeta_0} \quad (\text{where } \zeta = T, B, n).$$

n_0 , $\kappa_{\perp,0}$, and $\kappa_{\perp,0}$ represent the zeroth order electron number density, diffusive heat flow coefficient, and Righi–Leduc heat flow transport coefficient, respectively. The perturbed thermo-electric, δq_{TE} , heat

flow has been neglected here. δq_{TE} is significant in regions of both large magnetic field magnitude and gradient which occur close to the ablation surface in the 400 T simulation (green line in Fig. 8), but is negligible in all other conditions simulated here. The convective transport of heat, $v_{x,0}\partial_x\delta T$ and terms of order $\mathcal{O}(\partial\kappa_{\perp,0}/\partial\chi)$ and above have also been neglected, which are also found to be small.

The change of variables $\delta u = T_0^{5/2}\delta T$ is made, and the perturbation x dependence is assumed to take the form, $\delta u = \delta u_0 \exp(k_x x)$ and $\delta B_z(x) = \delta B_z \exp(k_x x)$. It is then possible to find the spatial eigenmodes, k_x , of this system, which are well approximated by

$$k_x \approx \left(\frac{(\delta_1\gamma_1 - \epsilon_1\eta_1)}{\delta_2\gamma_3} \right)^{1/4} \approx \xi k \left[1 + \frac{1}{\alpha_0 k^2} \left(\partial_x C_{x,0} - \frac{\partial\beta_{\wedge,0}}{\partial\chi} \theta_0 - \frac{\partial\kappa_{\wedge,0}}{\partial\chi} \frac{\theta_0 l_n}{\kappa_{\perp,0}} \right) + \frac{i}{\kappa_{\perp,0}\alpha_0 k} \frac{\partial\kappa_{\wedge,0}}{\partial\chi} \tau_{ei,0} n_0 B_{z,0} (l_B - l_n) \right]^{1/4}, \quad (11)$$

where $\xi = +1, -1, +i, -i$. A full derivation of Eq. (11) and the related δu and δB_z eigenfunctions is given in the Appendix. The first term in the numerator represents the coupling between magnetic field amplification and damping (caused by the Nernst effect, frozen in flow and resistivity) and the diffusive damping of temperature perturbation. The second term in the numerator, $\epsilon_1\eta_1$, is the instability or mode inversion source term, the coupling between spontaneous generation of magnetic field by the Biermann-battery effect, η_1 , and the Righi-Leduc heat flow, ϵ_1 .

The magnitude and phase of k_x vary depending on the degree of magnetization. If all magnetic field effects are neglected, Eq. (8) reduces to a diffusion equation describing thermal smoothing of δT via diffusive thermal conduction, $k_x \rightarrow k$. This limit describes the exponential attenuation of δT_e with distance into the conduction zone, sometimes referred to as the ‘‘cloudy day’’ thermal smoothing model.^{30,31}

The coupling between Righi-Leduc and self-generated fields, $\epsilon_1\eta_1$, is pivotal in the perturbation evolution. $\epsilon_1\eta_1$ changes sign

depending on whether χ is less than or greater than ~ 0.1 (this threshold depends on Z through its dependence on $\frac{\partial\kappa_{\wedge,0}}{\partial\chi}$).

For $\chi \gtrsim 0.1$, as is the case in the 400 T simulation, $\frac{\partial\kappa_{\wedge,0}}{\partial\chi} < 0$ and $\epsilon_1\eta_1 > 0$ (according to local predictions),¹³ and this term results in a smaller k_x and thus either slower δT_e or δB_z damping or growth due to field-generating thermal or magneto-thermal instabilities.

In the opposing limit (relevant for 0 and 50 T), $\epsilon_1\eta_1 < 0$. In this case, the $\epsilon_1\eta_1$ term acts to damp the incumbent δT . Unlike conventional damping, the damping term is driven by the 10–100 fold δB amplification by the Nernst effect within the conduction zone. Instead of returning to zero, the δT_e overshoots and inverts,⁹ seen in the green and red curves of Fig. 4(b). In the Appendix, analysis of the system eigenmodes is used to show that δT_e perturbation is composed of both a decaying and an oscillatory component, the latter of which is responsible for this phase inversion.

D. Non-locality and magnetic field self-generation and Righi-Leduc heating

In Sec. IV C, we explored how the limits of δT_e (and therefore δP) evolution, instability and ‘‘overdamping,’’ are governed by the interplay between $\delta q_{RL,y}$, $\partial_t B$ generation and the Nernst advection of the B-field.

In this section, we investigate the manner in which non-locality may affect these two sides of the magneto-thermal and field-generating thermal instability feedback loops. Figures 5 and 6 display color maps of the perturbed Hall parameter $\delta\chi = \chi - \langle\chi\rangle$ overlaid with contours of Righi-Leduc heating, $\partial_y q_{y,RL}$, and magnetic field amplification and advection, due to the Biermann and cross-gradient Nernst term, $\partial_t B_{z,1}$, given by the expression

$$\begin{aligned} \partial_t \mathbf{B} &= \nabla \times \left(\frac{\nabla P_e}{en_e} + \frac{1}{e} \beta^e \cdot \nabla T_e \right) \\ &= - \frac{\nabla n_e \times \nabla T_e}{en_e} + \nabla \times (\mathbf{v}_{\wedge} \times \mathbf{B}), \end{aligned} \quad (12)$$

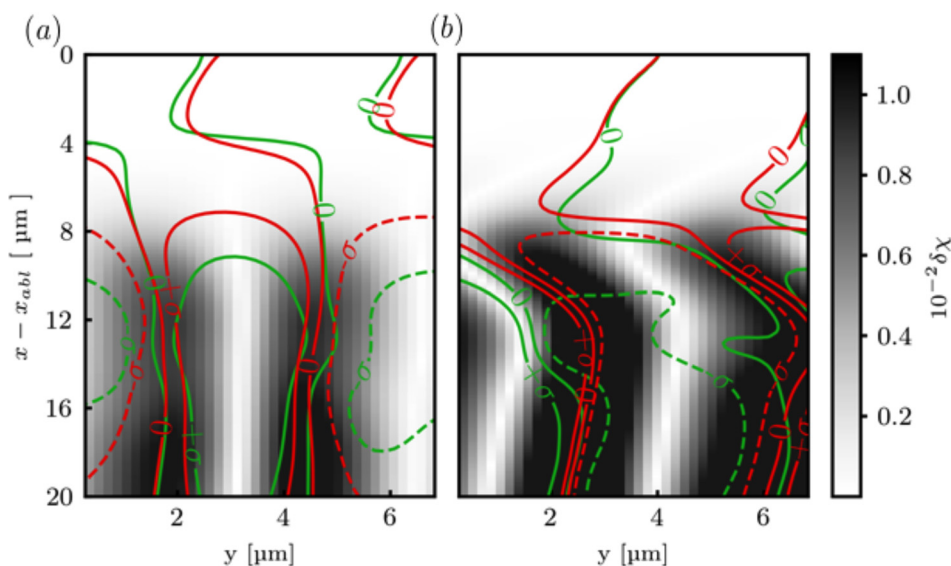


FIG. 5. Image plots of $\delta\chi$ within the conduction zone with $\partial_y q_{y,RL}$ contours overlaid for simulations with 50 (left) and a 400 T (right) applied magnetic fields. Three contours are plotted: $-\sigma$, 0, and $+\sigma$. Red and green contours are values for $\partial_y q_{y,RL}$ reconstructed from IMPACT simulations and as predicted by a local model, respectively.

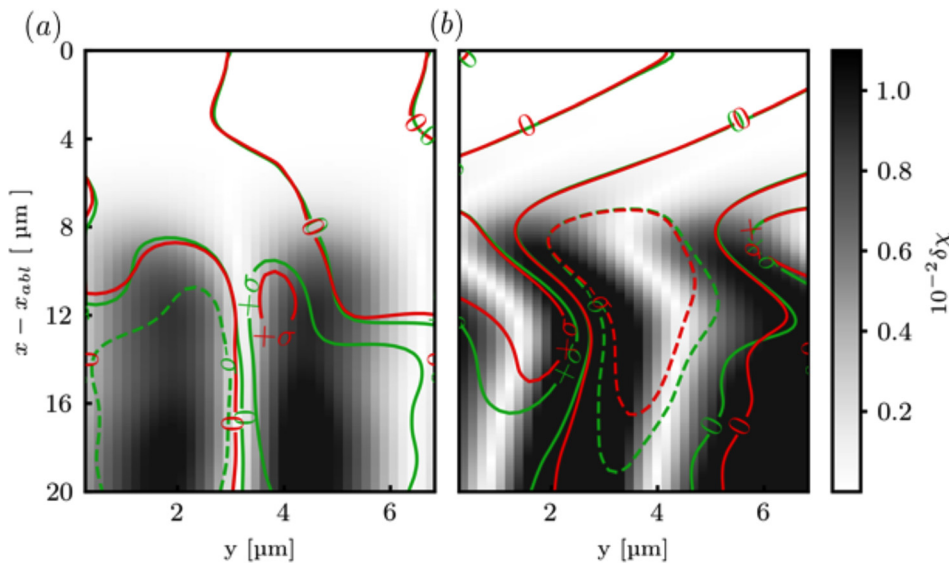


FIG. 6. Image plots of $\delta\chi$ within the conduction zone with $\partial_t \mathbf{B}$ contours overlaid for simulations with 50 (left) and a 400 T (right) applied magnetic fields. Three contours are plotted, $-\sigma$, 0, and $+\sigma$, red is kinetic (reconstructed from IMPACT simulations) while green is the local predictions for $\partial_y q_{y,RL}$.

where $\mathbf{v}_\wedge = \frac{\beta_e}{e|\mathbf{B}|} \nabla T_e$. Figures 5(a) and 6(a) correspond to a 50 T applied field simulation while Figs. 5(b) and 6(b) correspond to a 400 T simulation. Green contours are the predicted values for $\partial_y q_{RL,y}$ and $\partial_t B_z$ given by a local model, while red contours are those of the true non-local values, reconstructed from the IMPACT simulations.

The 50 and 400 T simulations show several key differences. In the 50 T case, at the peak of the temperature gradient, the term $d_y q_{RL,y}$ heats the $\delta\chi$ troughs (i.e., is π out of phase with $\delta\chi$), causing δT to invert. In the 400 T case this term heats in phase with $\delta\chi$ and so instead of inversion we observe growth of the incumbent δT . Further into the conduction zone, contours of $\partial_t B_z$ and $\partial_y q_{y,RL}$ twist, shifting in the y direction, due to a combination of $v_{N,\wedge}$ magnetic field advection and the $\partial_x B_z$ and $\partial_x n_0$ driven Righi-Leduc heat flow $q_{RL} \propto ik \frac{\partial \kappa_{\wedge 0}}{\partial \chi} \tau_{ei,0} n_0 B_{z,0} (l_B - l_n)$.

Comparison of green (local) and red (non-local) contours demonstrates that Righi-Leduc heating is larger in a non-local model for both applied field strengths (the $+\sigma$ and $-\sigma$ contours extend over a

much wider area). A possible explanation for this is that the Righi-Leduc heat flow is mediated by a more magnetized hot electron population [$\chi = \omega \tau_{ei}(v) \propto v^3$]. Therefore, the electron deficit in the f_0 tail is compensated for by an increase in effective magnetization, resulting in a net $q_{y,RL}$ enhancement even at the top of the temperature gradient. Biermann field generation and cross-gradient Nernst advection, on the other hand, are reduced by non-locality in regions of flux-suppression.

Close to the ablation surface, non-local and local contours of $\partial_y q_{RL,y}$ are offset in the 50 T simulation [Fig. 5(a)], but nearly exactly overlap in the 400 T simulation [Fig. 5(b)]. This is likely due to the strong magnetic field at $x \sim x_{abl}$ localizing $q_{RL,y}$, consistent with results seen in Fig. 3.

E. The effect of non-locality on the transverse heat flow

Non-locality changes both the magnitude and direction of the heat flux. The latter is investigated in this section. Correct determination of heat flux direction is important as the relative degree of transverse heat flow governs both the thresholds for instability and thermal smoothing magnitudes.

Non-local modification of the heat flow and Nernst-effect directions is primarily due to two mechanisms here. The first is that originally studied by Epperlein *et al.* in VFP simulations without B-fields.³² Hot, long λ_{mfp} electrons are only sensitive to relatively long scale length changes in plasma temperature and collisionality. These long λ_{mfp} electrons are relatively unperturbed by the local, short scale length, modulations in the transverse direction compared to bulk gradients. The resultant heat flow and Nernst effects are directed much further down the bulk temperature gradient, shown schematically in Fig. 7. The Righi-Leduc heat flow, which is $q_{RL} \propto -(\mathbf{b} \times \nabla T_e)$, rotates in the opposite direction (further toward the transverse direction). Furthermore, in regions of preheat, effects of non-locality reverses the roles of the arrows: q_\perp and v_N are enhanced and rotated further in the transverse direction while q_{RL} is enhanced and rotated

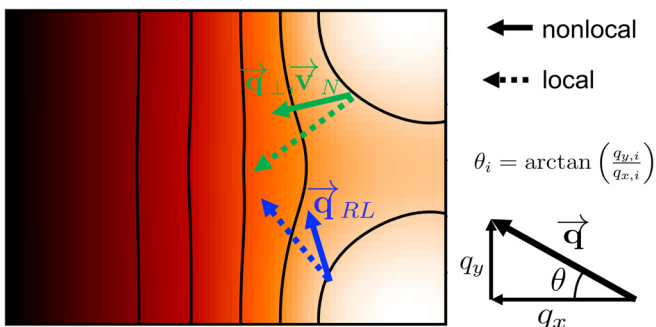


FIG. 7. Schematic showing the manner in which non-locality rotates and changes the magnitudes of different transport terms q_\perp , v_N , and q_{RL} . In regions of preheat, the dashed and solid arrows reverse in characteristics—the Nernst and diffusive heat flow become larger and further toward the transverse direction than their equilibrium counterparts, while the Righi-Leduc heat flow becomes larger and rotates further down the temperature gradient.

further down the temperature gradient. The rotation displayed in Fig. 7 applies for cases of low magnetization (0 and 50 T). For larger applied field strengths, non-local direction changes are controlled by the second mechanism.

The second mechanism is caused by the differing magnetization of hot electron populations (relative to the thermal Hall parameter). Magnetic field changes the magnitude of coefficients within, the transport tensors of Eq. (3); hence, a changing effective magnetization will also alter the prevailing direction of heat flux and Nernst advection.

The change of direction in turn acts to alter the phase of δq . Figure 8 displays lineouts of δq for the different heat flow components. The degree to which non-locality shifts the phase of different δq_y components is a function of the distribution function shape and their relative sensitivity to magnetization effects. Two characteristic points in the conduction zone are selected, for two different strengths of externally applied magnetic field: 0 and 400 T. Figures 8(a) and 8(d) correspond to the region of preheat and Figs. 8(b) and 8(e) to a point of “heat flux-suppression” at the top of the temperature gradient.

As expected, δq exhibits non-local suppression and enhancement in all heat flow components in regions of flux-suppression and preheat, respectively, for 0 T simulations. The same is not true in the 400 T simulation. The perturbed Righi–Leduc heat flow shows non-local enhancement of its amplitude even in regions of flux-suppression. Meanwhile, non-locality has shifted the relative phase of δq for various heat flow components. In the most extreme example, the non-local δq_y (solid black line) is directed in the opposite direction

to local predictions (dashed black line) for the 400 T simulation at the top of the temperature gradient, Fig. 8(e).

V. SUMMARY AND CONCLUSIONS

There has been growing interest in performing laser-ablation experiments that involve a pre-applied magnetic field, for example, in the context of using magnetic field to boost the yield of inertial confinement fusion experiments.¹ Here, the conduction zone is critical to transporting laser energy from where it is absorbed by the plasma to the ablation front; however, heat transport in this region is non-local, requiring kinetic simulation. We have performed the first two-dimensional Vlasov–Fokker–Planck simulations of the conduction zone of pre-magnetized ICF targets, to gain insights into the evolution of the magnetic field and heat flow. The Nernst effect rapidly cavitates the conduction zone magnetic field, as a consequence only relatively modest $\omega\tau_{ei} \lesssim 0.2$ Hall parameters are achieved in these simulations. As a consequence, the onset of magneto-thermal⁴ and Tidman–Shanny³³ instabilities is inhibited in simulations presented here, even for large applied magnetic field strengths (up to 400 T). In the low magnetization limit, the Righi–Leduc heat flows down gradients of Hall parameter, inverting an applied transverse (to the temperature gradient) perturbation and causing its amplitude to oscillate with distance into the conduction zone. In the high magnetization limit, the Righi–Leduc heat flow behaves as a source term for the magneto-thermal and Tidman–Shanny instabilities. $\delta q_{RL,y}$ instead directs heat toward $\delta\chi$ peaks, competing with the damping effects of diffusive thermal conduction to increase the δT amplitude. For the 400 T

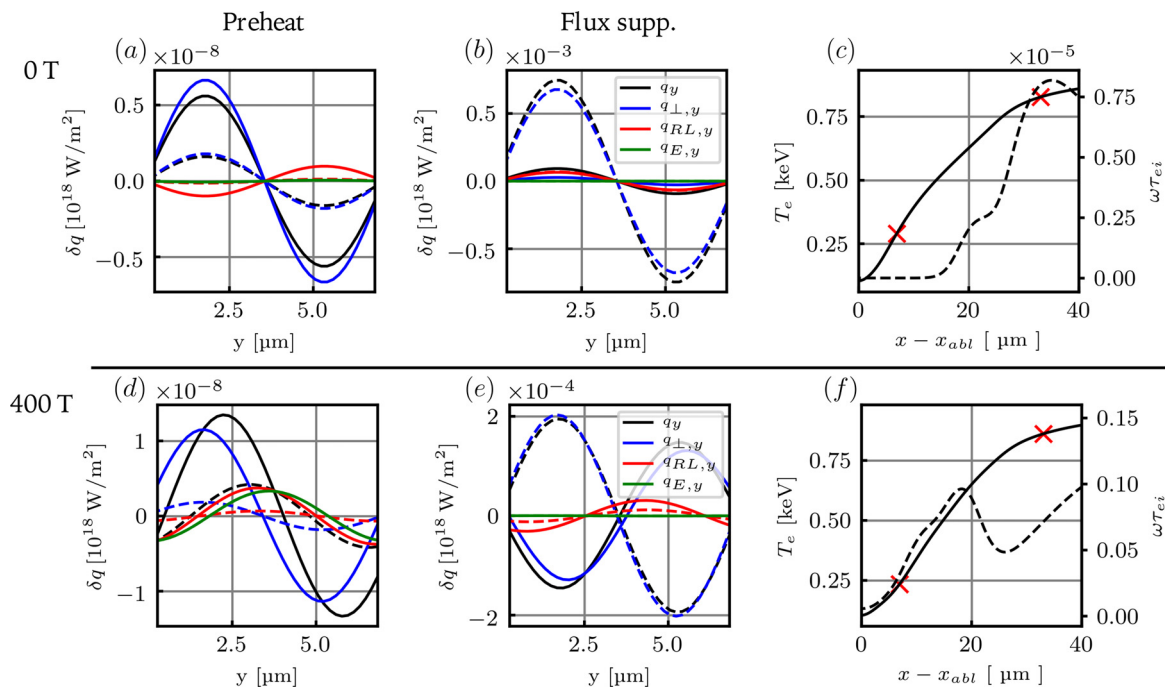


FIG. 8. Lineouts of δq , at different positions in the conduction zone—(a) and (d) in a region of preheat, (b) and (e) in a region of flux-suppression, sampled at positions marked by the left and right crosses on the temperature gradient in (c) and (f), respectively. Solid lines represent kinetic predictions for each heat flow component while dashed lines represent local thermodynamic equilibrium components. In (a), δq_y (solid blue line) is both enhanced and shifted out of phase by $-\pi/2$ relative to the local prediction, dashed blue line, while in (b) heat flow is suppressed.

simulation, this results in both the suppression of phase inversion and a larger ablation surface δT_e relative to 0 and 50 T. However, a net growth in δT , caused by instability, does not occur.

Non-local effects alter these processes. The hot, relatively collisionless electrons ($\lambda_{mfp} \propto v^4$, where v is the electron velocity) stream down the temperature gradient resulting in a hot electron population deficit close to the critical surface and an enhanced population at the ablation surface. As a rule of thumb, this fast-electron population surplus and deficit causes a corresponding increase and reduction in the extended-magnetized transport terms, including Nernst, diffusive heat flow and Biermann battery magnetic field spontaneous generation/cross-gradient Nernst advection. However, this general rule is not always true when an applied magnetic field is present. For large applied magnetic fields, the magnetic field is advected toward the ablation surface and compressively amplified, relocalizing transport in this region. Meanwhile, the Hall parameter scales with the electron velocity, $\omega\tau_{ei} \propto v^3$. For magnetized transport terms (e.g., $q_{y,RL}$ ²⁶) mediated by high velocity, more magnetized electrons, the *effective magnetization* of the plasma transport may be much higher than the thermal electrons' Hall parameter. In the 50 T simulation, this effect results in an enhanced $q_{RL,y}$ relative to local models, even at the top of the temperature gradient, in the region typically assigned for flux-suppression.

The evolution of the magnetic field and perturbations in the magnetic field that we have studied here have clear relevance to magnetized ICF implosions, motivating the inclusion of a kinetic model of all the relevant magnetic field evolution terms (and their effect on the heat flow) in integrated simulations. The use of a fully kinetic model (such as VFP) in this context is outside the scope of current computational resources. While reduced non-local models which include magnetic fields and can be used in integrated calculations exist, their accuracy has yet to be comprehensively determined through comparison to fully kinetic simulations. It therefore remains important to understand the variety of ways in which non-locality may modify transport from predictions made using conventional hydrodynamics modeling of full, integrated simulations of magnetized ICF implosions.

ACKNOWLEDGMENTS

D.W.H., C.P.R., and R.J.K. would like to acknowledge funding from the UK Engineering and Physical Sciences research council (Grant No. EP/M011372/1). This work has been carried out within the framework of the EUROfusion Consortium and has received funding from the Euratom research and training program 2014–2018 under Grant Agreement No. 633053 (Project Reference CfP-AWP17-IFE-CCFE-01). The views and opinions expressed herein do not necessarily reflect those of the European Commission.

APPENDIX: LINEAR THEORY

Linear perturbation theory may be used to describe the conduction zone spatial evolution of δT_e . Starting with the steady-state temperature equation, subject to sinusoidally perturbed heating, $\nabla \cdot \mathbf{q} = I\delta(x - x_c)$, assuming harmonic perturbations in temperature and magnetic field of the form

$$\delta T \propto \delta T e^{iky + i\omega t + k_x x}, \quad (\text{A1})$$

$$\delta B_z \propto \delta B_z e^{iky + i\omega t + k_x x}, \quad (\text{A2})$$

the following linearized temperature and magnetic field equations are arrived:

$$(\delta_1 + \delta_2 \partial_x^2) \delta u + \epsilon_1 \delta B_z = 0, \quad (\text{A3})$$

$$(\eta_1 + \eta_2 \partial_x + \eta_3 \partial_x^2) \delta u + (\gamma_1 + \gamma_2 \partial_x + \gamma_3 \partial_x^2) \delta B_z = 0, \quad (\text{A4})$$

where the coefficients are defined as follows:

$$\delta_1 = -\kappa_{\perp,0} k^2 + ik \frac{\partial \kappa_{\perp,0}}{\partial \chi} \tau_{ei,0} n_0 B_{z,0} (l_B - l_n), \quad (\text{A5})$$

$$\delta_2 = \kappa_{\perp,0}, \quad (\text{A6})$$

$$\eta_1 = \frac{ik}{T_0^{5/2}} l_n + \alpha_0 \frac{B_{z,0}}{T_0^{7/2}} \left(\frac{15}{2} l_T l_B - \frac{3}{2} l_{2,T} \right) + \frac{\partial \beta_{\perp,0}}{\partial \chi} \frac{\tau_B B_{z,0}}{n_0 T_0} (k^2 + l_B l_T - l_n l_T - 2l_T^2 + l_{2,T}), \quad (\text{A7})$$

$$\eta_2 = -\frac{3}{2} \alpha_0 \frac{B_{z,0}}{T_0^{7/2}} l_B + \frac{\partial \beta_{\perp,0}}{\partial \chi} \frac{\tau_B B_{z,0}}{n_0 T_0} (2l_T + l_n - l_B), \quad (\text{A8})$$

$$\eta_3 = -\frac{\partial \beta_{\perp,0}}{\partial \chi} \frac{\tau_B B_{z,0}}{n_0 T_0}, \quad (\text{A9})$$

$$\epsilon_1 = -ik \frac{\partial \kappa_{\perp,0}}{\partial \chi} \theta_0 T_0^{5/2}, \quad (\text{A10})$$

$$\gamma_1 = \left[\partial_x C_{x,0} + \alpha_0 k^2 - \frac{\partial \beta_{\perp,0}}{\partial \chi} \partial_x \theta_0 \right],$$

$$\gamma_2 = \left[C_{x,0} - \frac{\partial \beta_{\perp,0}}{\partial \chi} \theta_0 + \frac{3}{2} \alpha_0 \frac{\partial_x T_0}{T_0} \right],$$

$$\gamma_3 = -\alpha_0,$$

where

$$\alpha_0 = \frac{\alpha_{\perp,0} \delta_c^2}{T_0^{3/2}}, \quad \theta_0 = \tau_{ei,0} \partial_x T_0,$$

$$l_{\zeta} = \frac{\partial_x \zeta_0}{\zeta_0}, \quad \text{and} \quad l_{2,\zeta} = \frac{\partial_x^2 \zeta_0}{\zeta_0} \quad (\text{where } \zeta = T, B, n).$$

The eigenmodes of this system are given by the quartic equation

$$\delta_2 \gamma_3 k_x^4 + \delta_2 \gamma_2 k_x^3 + (\delta_1 \gamma_3 + \delta_2 \gamma_1 - \epsilon_1 \eta_3) k_x^2 + (\delta_1 \gamma_2 - \epsilon_1 \eta_2) k_x + (\delta_1 \gamma_1 - \epsilon_1 \eta_1) = 0. \quad (\text{A11})$$

For the case $l_B > l_T$, the k_x^3 , k_x^2 , and k_x coefficients are small and Eq. (A11) has the following approximate solutions:

$$k_x \approx \left(\frac{(\delta_1 \gamma_1 - \epsilon_1 \eta_1)}{\delta_2 \gamma_3} \right)^{1/4} \approx \zeta k \left[1 + \frac{1}{\alpha_0 k^2} \left(\partial_x C_{x,0} - \frac{\partial \beta_{\perp,0}}{\partial \chi} \theta_0 - \frac{\partial \kappa_{\perp,0}}{\partial \chi} \frac{\theta_0 l_n}{\kappa_{\perp,0}} \right) + \frac{i}{\kappa_{\perp,0} \alpha_0 k} \frac{\partial \kappa_{\perp,0}}{\partial \chi} \tau_{ei,0} n_0 B_{z,0} (l_B - l_n) \right]^{1/4}, \quad (\text{A12})$$

where $\zeta = +1, -1, +i, -i$. The first term in the numerator represents the coupling between magnetic field amplification and damping (caused by the Nernst effect, frozen in flow and resistivity) and the diffusive damping of the temperature perturbation. The second term is the instability or mode inversion source term, composed of the coupling between spontaneous generation of magnetic field by

the Biermann battery effect and the Righi–Leduc heat flow. The final term on the right-hand side is responsible for shifting the phase of δT_e , and is negligible in 50 T simulations except for regions close to the ablation surface.

In the limit that all magnetic field and hydrodynamic effects are neglected, the cloudy day model is recovered $k_x \rightarrow k$.³⁵

For the case of Dirichlet boundary conditions bounding the conduction zone, $\delta T(x_c) = \delta T_c$ and $\delta B_z(x_c) \rightarrow \delta B_{z,c}$, and $\delta T(x_c) \rightarrow 0$, $\delta B_z(x_a) \rightarrow 0$ at the ablation surface (suitable for early times) and we find that eigenvalues in Eq. (11) yield the solution,

$$\delta T_e = (c_{1,r} + ic_{1,i}) \sinh(k_x x) + (c_{2,r} + ic_{2,i}) \sin(k_x x), \quad (A13)$$

where

$$c_{1,r} = \frac{1}{2k_x^2 T_0^{5/2}} (k_x^2 - k^2) u_c \operatorname{sech}(k_x x_c), \quad (A14)$$

$$c_{1,i} = \frac{\delta B_{z,c} \kappa_{\perp,0}}{2k_x^2 \zeta T_0^{5/2}} (k_x^4 - k^4) \operatorname{sech}(k_x x_c), \quad (A15)$$

$$c_{2,r} = \frac{\delta B_c \kappa_{\perp,0}}{2k_x^2 \zeta T_0^{5/2}} (k^4 - k_x^4) \operatorname{sech}(k_x x_c), \quad (A16)$$

$$c_{2,i} = \frac{1}{2k_x^2 T_0^{5/2}} (k^2 + k_x^2) u_c \operatorname{sech}(k_x x_c), \quad (A17)$$

where $\zeta = -ic_1$.

DATA AVAILABILITY

The data that support the findings of this study are openly available in the York Research Database at <http://doi.org/10.15124/4084a07d-9ba6-49a1-9133-afe26d87625f>, Ref. 34.

REFERENCES

- ¹P. Y. Chang, G. Fiksel, M. Hohenberger, J. P. Knauer, R. Betti, F. J. Marshall, D. Meyerhofer, F. H. Séguin, and R. D. Petrasso, “Fusion yield enhancement in magnetized laser-driven implosions,” *Phys. Rev. Lett.* **107**, 035006 (2011).
- ²S. I. Braginskii, “Transport processes in a plasma,” *Rev. Plasma Phys.* **1**, 205 (1965).
- ³A. Fruchtman and H. R. Strauss, “Thermomagnetic instability in a magnetized plasma,” *Phys. Fluids B* **4**, 1397–1400 (1992).
- ⁴J. J. Bissell, C. P. Ridgers, and R. J. Kingham, “Field compressing magnetothermal instability in laser plasmas,” *Phys. Rev. Lett.* **105**, 175001 (2010).
- ⁵A. R. Bell, R. G. Evans, and D. J. Nicholas, “Electron energy transport in steep temperature gradients in laser-produced plasmas,” *Phys. Rev. Lett.* **46**, 243–246 (1981).
- ⁶E. M. Epperlein and A. R. Bell, “Non-local analysis of the collisional Weibel instability in planar laser-ablated targets,” *Plasma Phys. Controlled Fusion* **29**, 85–92 (1987).
- ⁷A. V. Brantov, V. Y. Bychenkov, W. Rozmus, C. E. Capjack, and R. Sydora, “Linear theory of nonlocal transport in a magnetized plasma,” *Phys. Plasmas* **10**, 4633–4644 (2003).
- ⁸C. P. Ridgers, R. J. Kingham, and A. G. R. Thomas, “Magnetic cavitation and the reemergence of nonlocal transport in laser plasmas,” *Phys. Rev. Lett.* **100**, 075003 (2008).
- ⁹D. W. Hill and R. J. Kingham, “Enhancement of pressure perturbations in ablation due to kinetic magnetized transport effects under direct-drive inertial confinement fusion relevant conditions,” *Phys. Rev. E* **98**, 021201(R) (2018).
- ¹⁰M. Sherlock and J. J. Bissell, “Suppression of the Biermann battery and stabilization of the thermomagnetic instability in laser fusion conditions,” *Phys. Rev. Lett.* **124**, 055001 (2020).
- ¹¹J. R. Davies, R. Betti, P. Y. Chang, and G. Fiksel, “The importance of electrothermal terms in Ohm’s law for magnetized spherical implosions,” *Phys. Plasmas* **22**, 112703 (2015).
- ¹²I. P. Shkarovsky, T. W. Johnston, and M. P. Bachynski, *The Particle Kinetics of Plasmas*, 1st ed. (Addison-Wesley Pub. Co., 1966).
- ¹³E. M. Epperlein and M. G. Haines, “Plasma transport coefficients in a magnetic field by direct numerical solution of the Fokker-Planck equation,” *Phys. Fluids* **29**, 1029 (1986).
- ¹⁴G. P. Schurtz, P. D. Nicolai, and M. Busquet, “A nonlocal electron conduction model for multidimensional radiation hydrodynamics codes,” *Phys. Plasmas* **7**, 4238–4249 (2000).
- ¹⁵P. D. Nicolai, J. L. Feugeas, and G. P. Schurtz, “A practical nonlocal model for heat transport in magnetized laser plasmas,” *Phys. Plasmas* **13**, 032701 (2006).
- ¹⁶W. Manheimer, D. G. Colombant, and V. N. Goncharov, “The development of a Krook model for nonlocal transport in laser produced plasmas. I. Basic theory,” *Phys. Plasmas* **15**, 083103 (2008).
- ¹⁷A. Marocchino, M. Tzoufras, S. Atzeni, A. Schiavi, P. D. Nicolai, J. Mallet, V. Tikhonchuk, and J.-L. Feugeas, “Comparison for non-local hydrodynamic thermal conduction models,” *Phys. Plasmas* **20**, 022702 (2013).
- ¹⁸J. P. Brodrick, R. J. Kingham, M. M. Marinak, M. V. Patel, A. V. Chankin, J. T. Omotani, M. V. Umansky, D. Del Sorbo, B. Dudson, J. T. Parker, G. D. Kerbel, M. Sherlock, and C. P. Ridgers, “Testing nonlocal models of electron thermal conduction for magnetic and inertial confinement fusion applications,” *Phys. Plasmas* **24**, 092309 (2017).
- ¹⁹M. Sherlock, J. P. Brodrick, and C. P. Ridgers, “A comparison of non-local electron transport models for laser-plasmas relevant to inertial confinement fusion,” *Phys. Plasmas* **24**, 082706 (2017).
- ²⁰J. F. Luciani, P. Mora, and J. Virmont, “Nonlocal heat transport due to steep temperature gradients,” *Phys. Rev. Lett.* **51**, 1664–1667 (1983).
- ²¹B. E. R. Williams, “Theory and modelling of fast electron transport in laser-plasma interactions,” Ph.D. thesis (Imperial College London, 2013).
- ²²R. J. Kingham and A. R. Bell, “Nonlocal magnetic-field generation in plasmas without density gradients,” *Phys. Rev. Lett.* **88**(4), 045004 (2002).
- ²³A. B. Langdon, “Nonlinear inverse bremsstrahlung and heated-electron distributions,” *Phys. Rev. Lett.* **44**, 575–579 (1980).
- ²⁴J. P. Brodrick, M. Sherlock, W. A. Farmer, A. S. Joglekar, R. Barrois, J. Wengraf, J. J. Bissell, R. J. Kingham, D. Del Sorbo, M. P. Read, and C. P. Ridgers, “Incorporating kinetic effects on Nernst advection in inertial fusion simulations,” *Plasma Phys. Controlled Fusion* **60**, 084009 (2018).
- ²⁵A. S. Joglekar, C. P. Ridgers, R. J. Kingham, and A. G. Thomas, “Kinetic modeling of Nernst effect in magnetized hohlraums,” *Phys. Rev. E* **93**, 043206 (2016).
- ²⁶T. H. Kho and M. G. Haines, “Nonlinear kinetic transport of electrons and magnetic field in laser-produced plasmas,” *Phys. Rev. Lett.* **55**, 825–828 (1985).
- ²⁷C. P. Ridgers, A. G. R. Thomas, R. J. Kingham, and A. P. L. Robinson, “Transport in the presence of inverse bremsstrahlung heating and magnetic fields,” *Phys. Plasmas* **15**, 092311 (2008).
- ²⁸J. J. Bissell, C. P. Ridgers, and R. J. Kingham, “Super-Gaussian transport theory and the field-generating thermal instability in laser-plasmas,” *New J. Phys.* **15**, 025017 (2013).
- ²⁹C. A. Walsh, J. P. Chittenden, D. W. Hill, and C. Ridgers, “Extended-magnetohydrodynamics in under-dense plasmas,” *Phys. Plasmas* **27**, 022103 (2020).
- ³⁰J. Nuckolls, L. Wood, A. Thiessen, and G. Zimmerman, “Laser compression of matter to super-high densities: Thermonuclear (CTR) applications,” *Nature* **239**, 139–142 (1972).
- ³¹V. N. Goncharov, O. V. Gotchev, E. Vianello, T. R. Boehly, J. P. Knauer, P. W. McKenty, P. B. Radha, S. P. Regan, T. C. Sangster, S. Skupsky, V. A. Smalyuk, R. Betti, R. L. McCrory, D. D. Meyerhofer, and C. Cherfils-Clerouin, “Early stage of implosion in inertial confinement fusion: Shock timing and perturbation evolution,” *Phys. Plasmas* **13**, 012702 (2006).

- ³²E. M. Epperlein, G. J. Rickard, and A. R. Bell, "Two-dimensional nonlocal electron transport in laser-produced plasmas," *Phys. Rev. Lett.* **61**, 2453–2456 (1988).
- ³³D. A. Tidman and R. A. Shanny, "Field-generating thermal instability in laser-heated plasmas," *Phys. Fluids* **17**, 1207–1210 (1974).
- ³⁴C. P. Ridgers and D. H. Hill (2021). "Vlasov-fokker-planck simulations of pre-magnetised ablating planar targets," The York Research Database.<http://doi.org/10.15124/4084a07d-9ba6-49a1-9133-afe26d87625f>
- ³⁵S. E. Bodner, "Rayleigh-taylor instability and laser-pellet fusion," *Phys. Rev. Lett.* **33**, 761–764 (1974).